ACS EARTH AND SPACE CHEMISTRY

http://pubs.acs.org/journal/aesccq

Article

Low-Temperature Specific Heat Capacity of Water−Ammonia Mixtures Down to the Eutectic

Bing Hong Chua, Elodie Gloesener, Mathieu Choukroun, Tuan H. Vu, Mohit Melwani Daswani,* Baptiste Journaux, Marshall J. Styczinski, and Steven D. Vance

Cite This: *ACS Earth Space Chem.* 2023, 7, 1971−1979

Read Online

ACCESS | Metrics & More | Article Recommendations | Supporting Information

ABSTRACT: Robust thermodynamic data are essential for the development of geodynamic and geochemical models of ocean worlds. The water−ammonia system is of interest in the study of ocean worlds due to its purported abundance in the outer solar system, geological implications, and potential importance for origins of life. In support of developing new equations of state, we conducted 1 bar specific heat capacity measurements (C_p) using a differential scanning calorimeter (DSC) at low temperatures (184−314 K) and low mass fractions of ammonia (5.2−26.9 wt %) to provide novel data in the parameter space most relevant for planetary studies. This is the first known set of data with sufficient fidelity to investigate the trend of specific heat capacity with respect to temperature. The obtained C_p in the liquid phase domain above the liquidus generally increases with temperature. Deviations of our data from the currently adopted equation of state by Tillner-Roth and Friend[Tillner-Roth, R.; Friend, D. G. *J. Phys. Chem. Ref. Data* **1998**, *27*, 63−96]. are generally negative (ranging from +1 to −10%) and larger at lower temperatures. This result suggests that suppression of the critical behavior of supercooled water (rapid increase in specific heat with decreasing temperature) by ammonia starts at a smaller concentration than that set by Tillner-Roth and Friend.[Tillner-Roth, R.; Friend, D. G.*J. Phys. Chem. Ref. Data***1998**, *27*, 63−96]. C_p measurements of the liquid were also obtained in the partial melting domain between the eutectic and liquidus. This novel data set will be useful in future investigations of conditions where such partial melt may exist, such as the ice shell−ocean boundary or the interiors of ocean worlds that may contain relatively large proportions of dissolved ammonia.

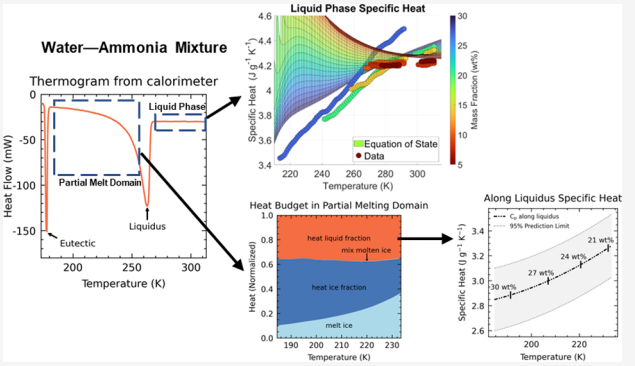

KEYWORDS: *calorimetry, ammonia−water, heat capacity, equation of state, ocean world interiors*

1. INTRODUCTION

The water−ammonia system is of significance for the geophysics of outer solar system bodies. Thermochemical models have suggested ammonia to be a substantial contributor to the volatile budget in gas giant subnebulae, with a water/ammonia mass ratio in the range of 1−15%,[2−4] and hydrothermally produced within planetary interiors.[5] It is also anticipated as a major compound in icy bodies.[6] Ammonia is inferred at Titan from in situ atmospheric measurements.[7] Ammoniated carbonates observed on the surface of Ceres imply a role for ammonia in its interior.[8] Ammonia has been detected as compound species on the surfaces of Ariel[9] and Charon[10] and on Kuiper Belt Objects;[11] as pure species in the plumes of Enceladus;[12] and as a product of ammonia-based chemical reactions in meteorites[13] and cometary materials.[14]

The presence of ammonia on icy ocean worlds has important implications for their geology, interior structure, and habitability. Ammonia dissolved in water reduces the density differential between liquid water and water ice, potentially promoting cryovolcanism.[15] Ammonia has anti-freeze properties, where partial melting of water ice proceeds between the eutectic point at 176 K (1 bar) and the liquidus curve. This heavy suppression of the melting point of water ice may be key to enabling persistent subsurface liquid oceans in the colder conditions of Titan, Europa, and Callisto.[16] Fixed or reduced nitrogen is integral in the abiotic synthesis of amino acids and C−H−O−N compounds.[17] In the reducing conditions commonly found in the outer solar system, it may be present in the form of ammonia[18] and may provide the source of fixed nitrogen for the potential origin of life.

The current commonly accepted representation of a water−ammonia equation of state is the Helmholtz formulation of Tillner-Roth and Friend.[1] This study highlighted inconsisten-

Received: April 10, 2023
Revised: August 15, 2023
Accepted: September 5, 2023
Published: September 21, 2023

cies in the isobaric heat capacity measurements that have been used for its construction. The heat capacities reported by Chan and Giauque[19] and Hildenbrand and Giauque[20] appeared inconsistent with the saturated enthalpies reported by Zinner.[21] Tillner-Roth and Friend included these data in the formulation, albeit with a low weight, because there were no other available low-temperature heat capacity measurements. Results from Chan and Giauque, Hildenbrand and Giauque, and Wrewsky and Kaigorodoff[22] were the only caloric data sets considered. Other calorimetric studies were either conducted at room temperature,[23] with very dilute mixtures,[24] or with sparse results.[25,26] To date, there are no extensive studies of isobaric heat capacity in the binary water−ammonia system at low temperatures and mass fraction conditions relevant to outer solar system planetary studies (0−5 GPa, 100−300 K, 0−15 wt %).[16] The poor coverage of data at this space is primarily due to difficulty in measuring low ammonia mass fraction samples due to its high volatilization capacity at surface Earth conditions and a heavier focus on higher mass fraction solution properties for absorption refrigeration applications.[27] As noted by Tillner-Roth and Friend,[28] the vapor−liquid equilibrium properties, being the most relevant, make up the majority of available data of the water−ammonia system. Now, we observe a growing interest in studying the icy moons, especially those that may contain water−ammonia, such as NASA's planned New Frontiers mission Dragonfly to Titan or the proposed Uranus Orbiter and Probe Flagship mission.[29] Hence, there is a renewed need to refine theoretical models of these bodies and, by extension, the thermodynamic database of the water−ammonia system.

Here, we report isobaric calorimetric measurements of the water−ammonia system conducted via differential scanning calorimetry at 1 bar pressure, between 184 and 314 K, at 5.2−26.9 wt %, covering a parameter space relevant to icy satellites (Figure 1). Isobaric heat capacity in the liquid phase above the liquidus is extracted directly from the calorimetric data, while a simple model is implemented to deconvolve the heat flows in the partial melting domain to extract heat capacity along the liquidus. After reporting the data, we compare our results with reported values in the literature and with Tillner-Roth and Friend's equation of state. We then discuss the applications of our data in future constructions of a water−ammonia equation of state and further implications for the thermodynamics of planetary bodies.

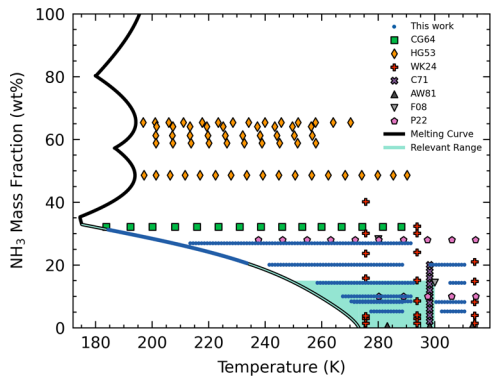

Figure 1. Mass fraction and temperature parameter space (at 1 bar) of the currently available isobaric calorimetric studies. This work improves upon the current data set and also introduces novel data in the parameter space most relevant for outer solar system planetary bodies, shown as the shaded region and the shaded line along the melting curve. CG64—Chan and Giauque;[19] HG53—Hildenbrand and Giauque;[20] WK24—Wrewsky and Kaigorodoff;[22] C71—Chernen'kaya;[23] AW81—Allred and Woolley;[24] F08—Fujita et al.;[25] and P22—Prieto-Ballesteros et al.[26]

2. EXPERIMENTAL METHODS

2.1. Experiment. Water−ammonia solutions were prepared using ammonium hydroxide (28.0−30.0 wt %, FCC/NF grade, Fisher Scientific) and pure liquid water (HPLC grade, VWR Chemicals) without further purification. The concentration of the stock ammonium hydroxide was first determined by identifying the liquidus of the solution based on the water ice partial melting endothermic peak and referencing that to the melting curve in the established 1 bar phase diagram.[16,30] 5 mL solutions of the desired ammonia mass fractions were then prepared via simple dilution and pipetted into the calorimeter's stainless steel cell, which has a capacity of 8.5 mL. The cell was then sealed by compressing a nickel gasket at 35 N m torque. With a 3.5 mL headspace, pressure change within the cell is negligible (ideal gas law suggests less than a factor of 2 change in headspace pressure), while the sample solution is free to expand and contract following phase transition and thermal expansion. Thus, the liquid−solid mixture is assumed to have been under approximately isobaric conditions throughout the experiments. Contributions of the air in the cell to the overall heat flux were considered and found to be negligible (see Supporting Information S1 for more details).

The experiments were carried out in similar fashion to previous work done by Vu et al.[31] The main apparatus used was a liquid-nitrogen-cooled Setaram BT 2.15 Calvet-type differential scanning calorimeter with an operational temperature range of 77−473 K. It houses two identical stainless steel cells within its calorimetric block, with one containing the sample and the other kept empty for reference. Each cell is connected to a thermopile equipped with a three-dimensional (3D) array of 64 thermocouples to measure the temperature differential between the cells over time, from which the heat flow can be obtained. The temperature profile of the experiment was preprogrammed using the accompanying Calisto software. The calorimeter was first cooled to approximately 120 K over a 24 h period, followed by a heating ramp at 0.1 K min $^{-1}$ to 300 or 320 K. A slow heating ramp is used to minimize errors introduced due to heat transfer hysteresis between the furnace and the calorimetric cells.[32] A blank run was also conducted with the sample cell kept empty over the same temperature profile. The corresponding heat flow was subtracted from the sample runs to correct for the small difference in response of the thermopiles. A full run took ∼72 h, and the calorimeter was evacuated for 24 h by a dry scroll pump after each run before proceeding with the next experiment. Table 1 shows a summary of the experiments and the associated parameters.

Due to the high vapor pressure of ammonia at ambient conditions, there were some volumetric losses of ammonium hydroxide out of the pipet during solution preparation, introducing unconstrained errors in ammonia mass fraction calculations. Independent measurements of the ammonia mass fraction were thus obtained for all of the samples by comparing the liquidus of the solution during the calorimetry runs to the literature. Typically, the peak−onset point of the water ice phase transition in a thermogram is used to determine the liquidus temperature, but as the partial melting curve is gradual

https://doi.org/10.1021/acsearthspacechem.3c00091
ACS Earth Space Chem. 2023, 7, 1971−1979

Table 1. Summary of Experimental Parameters

T_{end} (K)	m (g)	$T_{liquidus}$ (K)	w_{NH_3} (wt %)	w_{NH_3} error (wt %)
299.15	4.5858	262.5	8.4	0.3
	4.5202	259.6	10.0	0.2
	3.7778	207.4	26.912	0.002
319.15	4.5386	267.7	5.2	0.5
	4.1943	262.8	8.2	0.3
	3.8153	250.7	14.3	0.1
	3.7107	235.2	20.07	0.03

(Figure 2), this peak−onset signal is not well-defined. Instead, the minimum (endothermic) peak is taken as the liquidus

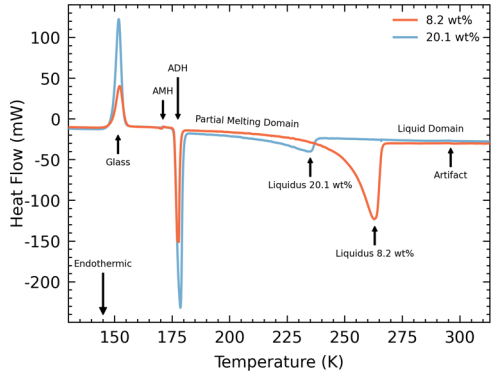

Figure 2. Two example thermograms at different ammonia mass fractions. Negative heat flows indicate endothermic processes. Phase transition points of glass crystallization, ammonia monohydrate (AMH) melting, ammonia dihydrate (ADH) melting at the eutectic, and composition-dependent liquidus points are noted. The partial melting domain and the liquid domain are constrained between the phase transition points. The slight kink at around 296 K is an artifact of the instrument and is observed on all experiments.

temperature for calibration to determine the ammonia mass fraction. A systematic temperature offset of the phase transitions measured by the calorimeter at a 0.1 K min $^{-1}$ ramp rate was reported to be +0.5 K[33] at 273.15 K. It is found that this accuracy is temperature-dependent, with ±0.02 K at the water−ammonia eutectic of 176 K (see Supporting Information S2 for more details). The measured liquidus temperatures were thus adjusted to account for this offset and then used as a reference against the established liquidus curve[30] to obtain the ammonia mass fractions.

The output data sets included time-series data of temperature and heat flow at intervals of 16.9 or 17.7 s depending on the temperature profile. Minute differences between the thermopiles induce a systematic artifact in the form of a kink in the data at around 296 K (Figure 2). This kink was also observed previously[31] and has negligible impact on the overall trend of the data. These erroneous data were removed. To correct for the large variability induced by instrument noise at the 16.9 or 17.7 s cadence, averages were taken at 1 K intervals with 3 K bin spacing. The standard deviation of each data point was used to represent uncertainties induced by the instrument noise.

The calorimeter was calibrated by measuring the heat flow in pure water ice samples. These data were then compared to theoretical heat flow values based on literature specific heat capacity data reported by Feistel and Wagner.[34] A linear correction function was fit to the relative deviations of heat flows with respect to the theoretical heat flow (Figure 3). Experimental data were then corrected.

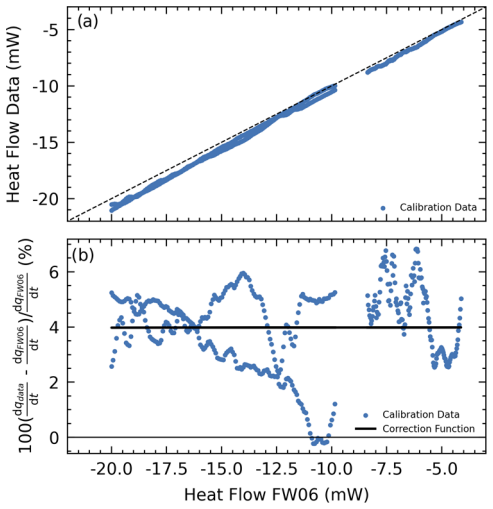

Figure 3. Calibration of the calorimeter heat flow. (a) Water ice heat flow data from 3 calorimetry runs against theoretical values by Feistel and Wagner.[34] (b) Deviation plot with the obtained linear calibration function used to correct raw experimental data.

2.2. Specific Heat Calculation. In the water−ammonia system, the thermograms covered multiple phase transitions. Thus, identification of the phase transitions was necessary to retrieve the specific heat capacity of the liquid solution. Two example thermograms are shown in Figure 2. At temperatures below the eutectic peak (176 K), the system is purely solid. Between the eutectic temperature at 176 K and the liquidus temperature (dependent on the ammonia mass fraction), the system is in a partial melting domain and exists as a mixture of liquid and pure water ice. The gradual endothermic curve (negative heat flow out of the system) indicates the gradual phase transition occurring in this domain. Above the liquidus to the maximum temperature of the profile, the system is purely liquid. After the heat flow values were corrected with the blank, specific heat capacities were calculated separately for the partial melting domain and the liquid domain.

In the liquid phase, all of the heat flow contributes to warming the solution. Hence, the (approximately) isobaric specific heat capacity (C_p) can be obtained via the following expression

$$C_p(T) = \frac{dq/dt}{m \times dT/dt} \quad (1)$$

where dq/dt is the measured heat flow, m is the mass of the sample, and dT/dt is the change in temperature over the corresponding time interval. At temperatures close to the liquidus, some heat flow values fall in the tail of the water ice melt endothermic peak. These were manually removed by visual inspection.

In the partial melting domain, four thermal processes participate in the total energetic budget along the liquidus line: (1) absorption of latent heat during melting of water ice, (2) absorption of latent heat to mix pure liquid water released by ice melting with the water−ammonia solution, (3) heating of the remaining fraction of water ice in the sample, and (4) heating of the liquid solution. The mass fraction of solid water ice (w^s) in the partial melting domain was obtained as a

https://doi.org/10.1021/acsearthspacechem.3c00091
ACS Earth Space Chem. 2023, 7, 1971−1979

function of temperature and overall ammonia mass fraction of the system via the lever rule

$$w^{s}(T) = \frac{w_{NH_3} - w^{l}_{NH_3}}{w^{s}_{NH_3} - w^{l}_{NH_3}} \quad (2)$$

for mass fraction of NH_3 in the system (w_{NH_3}), mass fraction of NH_3 in the liquid phase ($w^{l}_{NH_3}$), and mass fraction of NH_3 in the solid phase ($w^{s}_{NH_3}$), which is zero as the solid is pure water ice. Using the reported liquidus curve in the literature,[30] $w^{l}_{NH_3}$ was obtained at each temperature step to determine w^{s}.

The heat flow used in melting water ice ($dq_{melt}{}^{s}/dt$) is

$$\frac{dq^{s}_{melt}}{dt} = \frac{dw^{s}}{dt} m L_f(T) \quad (3)$$

where the latent heat of fusion of ice ($L_f(T)$) is a function of temperature. Along the liquidus of the water−ammonia system, melting proceeds incongruently, where the solid is pure water ice; hence, in the calculations, only the $L_f(T)$ of ice needs to be considered. $L_f(T)$ is the difference in enthalpies between water and ice I_h. The enthalpies were retrieved from SeaFreeze, a toolkit developed to describe the thermodynamic properties of water and water ice polymorphs.[35,36] SeaFreeze describes properties down to 240 K for only liquid water. As the dependence on temperature is approximately linear, required enthalpy values below this temperature were extrapolated.

The portion of heat that warms the water ice ($dq_{warm}{}^{s}/dt$) is

$$\frac{dq^{s}_{warm}}{dt} = w^{s}(T) m C^{s}_{p}(T) \frac{dT}{dt} \quad (4)$$

where the specific heat capacity of water ice ($C^{s}_{p}(T)$) is again a function of temperature. Literature-reported values for $C^{s}_{p}(T)$ are used.[34]

The portion of heat used in mixing of the solution with liquid water from the melted ice (dq_{mix}/dt) is

$$\frac{dq_{mix}}{dt} = \frac{dw^{s}}{dt} \frac{\delta H_{mix}}{\delta w^{l}_{NH_3}(T)} \quad (5)$$

for the change in the enthalpy of mixing corresponding to the change in ammonia mass fraction of the solution $\left(\frac{\delta H_{mix}}{\delta w^{l}_{NH_3}(T)}\right)$, which is obtained by applying a quadratic fit ($y = 18{,}743x^2 - 19{,}071x + 333$) to mixing enthalpy values (H_{mix}) reported by Staudt[37] (which can be found in Figure 14 of Tillner-Roth and Friend[1]) and then taking the difference of mixing enthalpy values corresponding to the change in liquid ammonia mass fraction. As the enthalpy of mixing becomes less negative with decreasing ammonia mass fraction, the process of mixing liquid water with solution in the partial melting domain is endothermic.

The heat flow used in warming the liquid solution can be calculated by subtracting all of the other contributions from the total measured heat flow. The specific heat capacity of the liquid along the liquidus can be derived by modifying the input heat flow in the numerator of eq 1

$$C_p(T) = \frac{dq/dt - dq^{s}_{melt}/dt - dq^{s}_{warm}/dt - dq_{mix}/dt}{m \times dT/dt} \quad (6)$$

Figure 4 shows the normalized heat decomposition of the system, highlighting heat requirements for each process. The

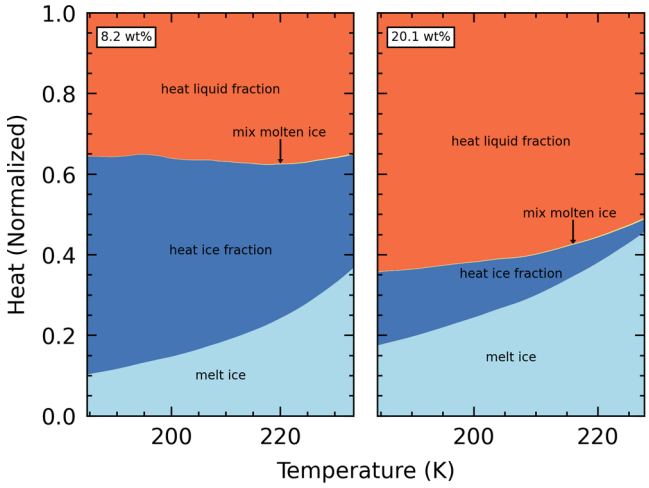

Figure 4. Two examples of energy budgets in the partial melting domain. Note the increase in energy required to melt the ice as partial melting proceeds with increasing temperature and the larger energy proportion required to warm the liquid at higher ammonia mass fractions.

heat used for mixing is minimal. At lower ammonia mass fractions, the proportion of heat required to warm the liquid is smaller, resulting in greater measurement uncertainties. This model is sufficiently robust at lower temperatures, where the system is assumed to be in equilibrium and phase transitions occur gradually. However, the slope of the liquidus increases with temperature, and water ice melts more rapidly per temperature step at a higher T. The system can no longer be assumed to be in equilibrium. Consequently, near the liquidus temperature, the model tends to overestimate the heat required to melt water ice, hence underestimating the specific heat capacity of the liquid. Beyond a certain temperature, specific heat values of the liquid start to decrease drastically. These were discarded by visual inspection. At temperatures close to the eutectic endothermic peak, some heat flow values fall in the tail of the peak. These were removed by visual inspection.

A Shomate equation[38] was used to fit the liquid phase C_p data:

$$C_p(T) = a + bT + cT^2 + dT^3 + \frac{e}{T^2} \quad (7)$$

Along the liquidus, a quadratic equation was used instead to avoid curve artifacts because of the large scatter in the C_p data.

2.3. Uncertainties. The temperature offset in determining liquidus temperatures resulted in ammonia mass fraction absolute uncertainties of 0.002−0.5 wt %, with higher ammonia mass fractions having lower uncertainties. Temperature and heat flow sensitivity of the calorimeter is ±0.1 mK and ±0.1 μW, respectively, and mass accuracy is ±0.1 mg. Combined with the uncertainty due to instrument noise, this gives a maximum propagated error for the liquid phase and along-liquidus C_p of <1.34% and <14.85%, respectively.

3. RESULTS AND DISCUSSION

3.1. Microscopic Observations. To assess the assumption of equilibrium in the partial melting domain of the water−ammonia system, microscopic images were obtained to observe

https://doi.org/10.1021/acsearthspacechem.3c00091
ACS Earth Space Chem. 2023, 7, 1971−1979

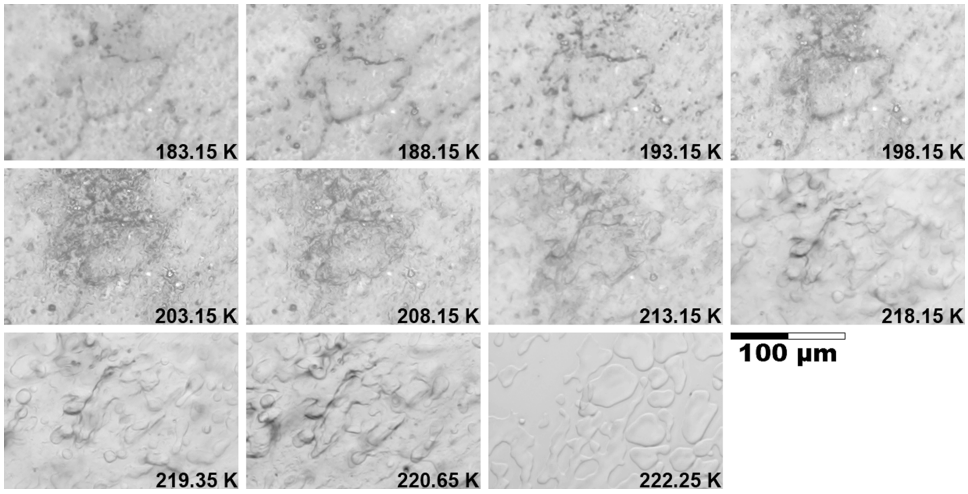

Figure 5. Microscopic images at 20× magnification for the water−ammonia solution (~23.6 wt % NH_3) in a cuvette slide in the partial melting domain. The water ice crystals melt in a homogeneous, gradual fashion, with no signs of crystal regrowth or melt migration. The system can be assumed to be in equilibrium throughout the phase transition.

the physical changes. A sample of solution (~23.6 wt % NH_3) was placed in a 0.1 mm well depth rectangular cuvette slide housed in a Linkam LTS350 cryostage. Temperature was initially cooled at 30 K min^{-1} to 123.15 K before heating at a ramp of 0.3 K min^{-1}. The evolution of the sample was surveyed throughout the ramp with an Olympus BX51 microscope equipped with a 20× objective and a DP74 camera. Stacked images were captured every 5 K or when noticeable changes were observed using the Olympus Stream image analysis software.

The microphotographs of the water−ammonia solution (~23.6 wt % NH_3) in the partial melting domain are shown in Figure 5. At 183 K, close to the eutectic, individual ice crystals can be identified as bright regions in the images. Individual water−ammonia pockets and liquids located along grain boundaries appear darker. As temperature increases, water ice melting proceeded in a homogeneous, gradual fashion, as evidenced by the growth of the darker regions. There were no visible signs of crystal regrowth or melt migration throughout most of the partial melting domain (up to ~218 K), while liquid pockets remained disconnected from one another. At temperatures closer to the liquidus (>218.15 K), the rate of melting increases rapidly until no crystals are left, and the migration of ice crystals occurs very quickly as well because the liquid becomes fully connected. These observations qualitatively support the assumption that the system is in equilibrium >5 K from the liquidus point, with no heterogeneities in crystallization or melt distribution at low liquid fractions. This finding also supports the reasoning that at temperatures close to the liquidus (within ~5 K), the system evolves too quickly for the equilibrium assumption to remain valid. Hence, the energy decomposition model can be applied, and C_p of the liquid along the liquidus can be extracted up to ~5 K from the liquidus point of each mixture.

3.2. Specific Heat Capacities. *3.2.1. Liquid Phase Specific Heat Capacity.* The specific heat capacities (C_p) in the liquid phase are listed in Figure 6a. C_p generally increases with temperature, and solutions with a higher ammonia mass fraction (w_{NH_3}) have steeper gradients. For 10.0 wt %, a decrease in gradient is observed approximately at 275 K. For 14.3 and 20.1 wt %, a decrease is observed approximately at

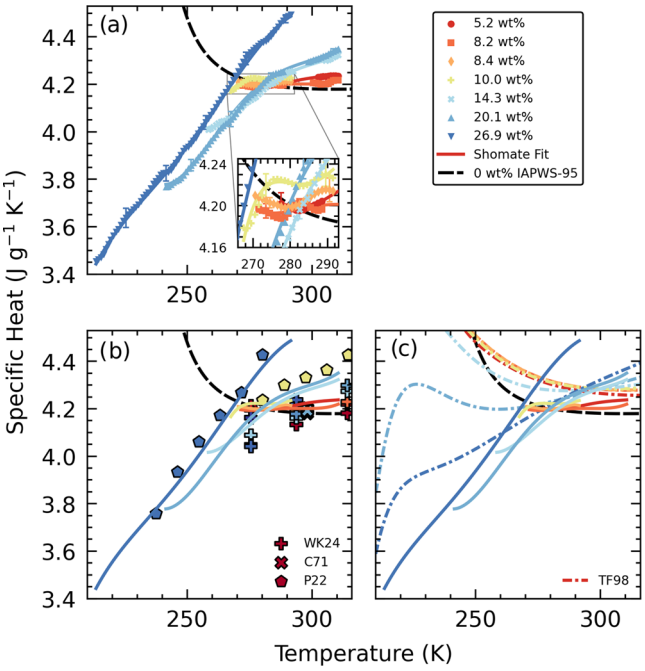

Figure 6. Specific heat capacities of the liquid phase above liquidus. (a) Plot of the experimental data. Markers represent 3 K bin-averaged data points, error bars represent 1σ errors of data points, and lines represent Shomate fits. (b) Plot of the Shomate fits with relevant literature values from Wrewsky and Kaigorodoff[22] (WK24), Chernen'kaya[23] (C71), and Prieto-Ballesteros et al.[26] (c) Plot of the Shomate fits with predicted values from Tillner-Roth and Friend[1] (TF98). The colors of the markers and lines represent the associated ammonia mass fraction. Specific heat capacities of pure water by Wagner and Pruß[39] (IAPWS-95) are shown as dashed lines.

290 K. Above 285 K, C_p is proportional to w_{NH_3}, with the exception of 5.2 wt %. The cause for this discrepancy is not immediately known due to the lack of reliable data between 290 and 300 K. Below 285 K, the higher w_{NH_3} C_p values cross below that of the lower w_{NH_3} due to the steeper C_p gradient. The predicted C_p of pure water from the IAPWS-95 equation of state[39] is also displayed to serve as a 0 wt % curve. In

https://doi.org/10.1021/acsearthspacechem.3c00091
ACS Earth Space Chem. 2023, 7, 1971−1979

general, C_P of water−ammonia solutions is slightly higher than that of water above 280 K.

These results are compared with relevant literature data from Wrewsky and Kaigorodoff,[22] Chernen'kaya,[23] and Prieto-Ballesteros et al.[26] (Figure 6b). The magnitudes of C_P generally agree, except for the 10 wt % data from Prieto-Ballesteros et al.,[26] which are consistent with our data at 280 K but slightly greater than our data at 288 K. Their 10 wt % C_p data are also higher than other literature values at higher temperatures, although differences in methodology and measurement procedures must be taken into account when evaluating these discrepancies between data. In this regard, they used an isothermal temperature step method and smaller sample volumes, which would reduce the thermal gradients during the measurements.[32] However, the air space inside the sample cell was larger than that in the present work, which could contribute to higher ammonia volatilization and consequently lower ammonia mass fraction in the solution. It would be useful to perform additional experiments in the future, comparing procedures to clarify these discrepancies.

There is a good alignment between the 28 wt % data from Prieto-Ballesteros et al.[26] and our 26.9 wt % data. The trends in C_P with respect to w_{NH_3} above 285 K are consistent. The crossover of the relationship between C_P and w_{NH_3} observed in our data is also observed by Wrewsky and Kaigorodoff.[22] Comparing with the currently adopted water−ammonia equation of state (EoS) devised by Tillner-Roth and Friend[1] (Figure 6c), differences become apparent. Figure 7 shows

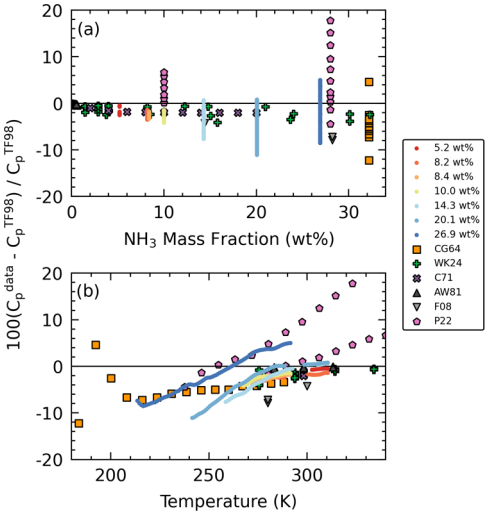

Figure 7. Deviations of specific heat capacities between equation-derived values and experimentally derived values, with (a) mass fraction and (b) temperature as the x-axis on the top and bottom plots, respectively. $y = 1$ indicates perfect alignment with the equation of state by Tillner-Roth and Friend.[1] Data from past C_P studies below the eutectic level are also included. Refer to Figure 1 for the abbreviations in the legend.

deviations of data from the EoS. Similar to other literature data, our C_P are generally smaller than the EoS predicted values, ranging from −10 to +1% for all samples except 26.9 wt %, which deviates up to +5%. Moreover, the crossover point between C_P and w_{NH_3} is predicted to be higher by ∼10 K.

Given the density of data points with respect to the temperature, a new observation can be made regarding the slopes of C_P along the temperature space. Our data show that C_P increases with temperature within the range of explored temperatures and composition. The Tillner-Roth and Friend EoS predicts a slower rate of increase at high concentrations (26.9 wt %). It also systematically predicts higher C_P for concentrations above 14.3 wt %. The deviations shown in Figure 7b illustrate this difference, with deviations decreasing in magnitude with respect to temperature. At higher temperatures >280 K, the slope tapers off and deviations stabilize. Shown in Figure 6c, C_P of pure water increases exponentially with decreasing temperature in the supercooled regime as temperature falls below 273.15 K. As the Tillner-Roth and Friend EoS is constructed with the IAPWS-95 water EoS,[39] this behavior of increasing C_P with decreasing temperature is also transposed onto water−ammonia mixtures. As w_{NH_3} increases, the effect is gradually suppressed and returns to the more typical increasing C_P behavior.

3.2.2. Along-Liquidus Specific Heat Capacity. In the partial melting domain (Figure 8), the composition of the liquid

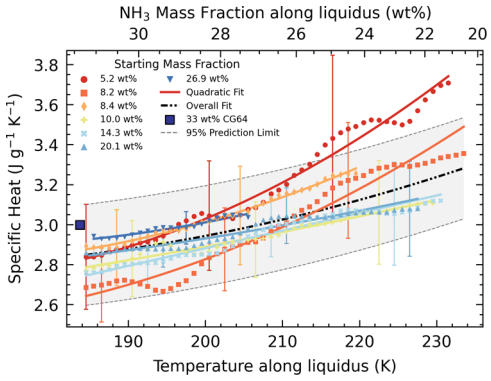

Figure 8. Specific heat capacities along the liquidus. Note that the ammonia mass fraction (w_{NH_3}) of the liquid follows the liquidus and is shown on the top x-axis; the labels indicate the starting ammonia mass fraction of the sample. The data point from Chan and Giauque[19] closest to the eutectic at 33 wt % falls within the 95% prediction interval of the overall quadratic fit.

follows the liquidus as temperature changes, regardless of the initial composition of the system; hence, the data sets represent the same liquid w_{NH_3} at each specified temperature. This behavior is represented with a secondary x-axis, indicating w_{NH_3} along the temperature range. There is general agreement of the C_P from the higher w_{NH_3} data sets. The lower w_{NH_3} data sets have greater C_P values that diverge more significantly at higher temperatures. Nevertheless, due to the larger uncertainties in the data, all of the data sets generally fall within 1σ uncertainty of each other. An overall quadratic fit of all data points was obtained, and this fit falls within 1σ of all of the data sets. The data point from Chan and Giauque[19] closest to the eutectic at 33 wt % falls within the 95% prediction interval of the overall fit.

Figure 9 combines C_P from along the liquidus with that in the liquid phase. The along-liquidus C_P values appear consistently lower than those above the liquidus. Ideally, the along-liquidus C_P should line up with liquid phase C_P at concentration-dependent liquidus points. However, due to the large prediction interval of the data, we are unable to conclusively calibrate the along-liquidus C_P.

https://doi.org/10.1021/acsearthspacechem.3c00091
ACS Earth Space Chem. 2023, 7, 1971−1979

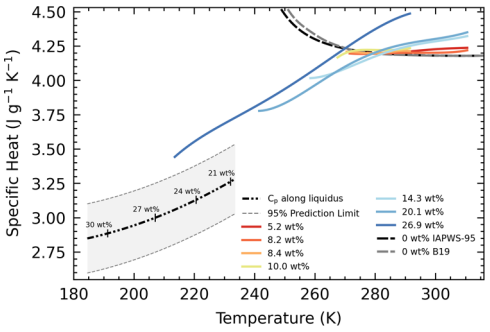

Figure 9. Specific heat capacities both along the liquidus and in the liquid phase. The decrease in the ammonia mass fraction along the liquidus is marked.

3.3. Implications for Planetary Applications.

3.3.1. New Equation of State Construction. When compared to our data, the Helmholtz formulation by Tillner-Roth and Friend[1] predicts higher C_P at low temperatures, with deviations up to −10% near the eutectic. This is in part due to the nature of the formulation, which is a combination of water and ammonia EoS. When predicting thermodynamic data below the melting point of water, the contributions from the water EoS consider pure water in the supercooled metastable regime. In the supercooled state, pure water displays a critical behavior where the heat capacity increases rapidly (Figure 6, black and gray dashed curves). This behavior has been linked to the transition from lower density to higher density configuration at low temperature.[40] As noted by Tillner-Roth and Friend, dissolved ammonia suppresses the critical behavior of water at low temperatures and higher concentrations, where C_P shows a typical decrease with decreasing temperature. The intensity of suppression of supercooled pure water critical behavior had to be arbitrarily chosen by Tillner-Roth and Friend, as no data were available at those conditions. Our results show that dissolved ammonia suppresses pure water critical behavior more effectively than what was predicted by Tillner-Roth and Friend. Even after considering 1σ error bars, the trends of our low mass fraction data are generally flat and do not carry the increasing specific heat trend observed in supercooled water (Figure 6). Hence, the data set suggests that the suppression of the supercooling effect starts at concentrations around or lower than approximately 5−10 wt %. However, future studies with lower mass fractions and larger temperature ranges are needed to refine the suppression of supercooled behavior by ammonia.

Currently, a new water−ammonia equation of state is under construction by Journaux et al.,[41] following the local basis function framework methodology.[42] In this framework based on the parametrization of the Gibbs free energy, experimental data of densities, specific heat capacities, and sound speed measurements are used to construct the representation. As C_P is linearly related to the partial derivative of Gibbs energy, it has a significant effect on the shape of the resultant Gibbs surface. The new C_P data from this work will directly inform such representation and will permit to better constrain the effect of dissolved ammonia, specifically at low concentrations, in depressing the critical behavior of supercooled pure water. Our 1 bar, low-temperature, low-ammonia-concentration C_P data will be a useful and novel contribution to the list of data sets. C_P data may also be used in other methodologies to derive fundamental potential representation of aqueous solutions.[1,36,43,44] Ultimately, a more accurate EoS can be constructed, and thermodynamic properties at low temperatures and low compositions can be retrieved for further applications, such as in planetary interior modeling.

3.3.2. Interior Models. In interior structure models of planetary bodies, an accurate representation of thermodynamic properties in relevant pressure and temperature conditions makes it possible to predict the temperature structure and phase transitions with depth. Changes to these properties, such as heat capacity, will alter the resulting profile structure. The only available models that include accurate NH_3 properties in the ocean[45] on Titan and Enceladus use NH_3 properties from the EoS by Tillner-Roth and Friend.[1] Generally, modeled temperatures of oceans within icy moons are below 300 K. Our results indicate that Tillner-Roth and Friend[1] overestimates C_P of low ammonia mass fractions. A more accurate model will have a lower ocean C_P, suggesting a marginally warmer adiabatic temperature profile that promotes a thicker ocean layer and a thinner high-pressure ice layer.

The latest iteration of the models by Vance et al.[45] (PlanetProfile[46]) was modified to test the first-order effects of the observed difference in C_P on Titan (see Supporting Information S3 for details). The percentage deviations of our 5.2 wt % data from the EoS by Tillner-Roth and Friend[1] (Figure 7) are extrapolated and applied to the ocean fluid. In the modeled temperature range of the ocean (255−261 K), relative deviations of C_P are between −3.8 and −1.8%. As the implementation of the water−ammonia EoS by Tillner-Roth and Friend in PlanetProfile is proprietary (REFPROP[47]), we opted to use a pure water model. Comparing with the unmodified pure water model, the model with the lower C_P has an ocean thickness that is 4.5 km greater, and the high-pressure ice thickness is correspondingly 4.5 km thinner.

This first-order comparison accounts for only a change in C_P. For a more accurate investigation, the change in C_P will affect the derived Gibbs surface, which will also alter other thermodynamic properties used in the models, such as density and thermal expansivity. With future development and implementation of a new water−ammonia EoS, such a test can be done in future studies.

At present, outer ice shells are typically modeled as pure ice I_h. For models with oceans containing NH_3, partial melting may be induced at the ice shell−ocean interface, as recently studied for aqueous ionic systems by Buffo et al.[48] and Vance et al.[49] These complexities involving NH_3 are yet to be modeled, and thermodynamic data in the partial melting domain are essential for their development. Our new reported C_P of the liquid in the partial melt regime will be useful in modeling thermodynamic conditions of melt pockets in ice shells.

4. CONCLUSIONS

In this work, we report new specific heat capacity data of the water−ammonia system at low temperatures (185−310 K) and low concentrations (5.2−26.9 wt %) relevant to predicted conditions in icy ocean worlds in our solar system. In the liquid phase, C_P follows a generally increasing trend with temperature. The critical behavior of supercooled water is not apparent in our data, suggesting a more intense suppression of this behavior by ammonia than predicted by Tillner-Roth and Friend.[1] Along the liquidus, a novel set of C_P measurements of the liquid have been extracted via decomposition of the various endothermic processes at play in the samples. Our data will be essential in ensuring the accuracy of a newly developed

https://doi.org/10.1021/acsearthspacechem.3c00091
ACS Earth Space Chem. 2023, 7, 1971−1979

equation of state in the low-temperature conditions most relevant to icy moons. Ultimately, accurate equations of state ensure robust interior models, which can then be used for further geophysical studies of the planetary bodies.

■ ASSOCIATED CONTENT

Supporting Information

The Supporting Information is available free of charge at https://pubs.acs.org/doi/10.1021/acsearthspacechem.3c00091.

Considerations of the contribution of air in the heat flux measurements (S1); figure of the systematic temperature offset of the phase transitions measured by the calorimeter and the associated fit (S2); table with the input parameters used in the PlanetProfile mode (S3); plotsfor each sample, including the thermogram, crystal fraction, calculated specific heat in the liquid phase and along-liquidus region and the energy budget in the along-liquidus region (S4) (PDF)

■ AUTHOR INFORMATION

Corresponding Author

Mohit Melwani Daswani − *Jet Propulsion Laboratory, California Institute of Technology, Pasadena, California 91109, United States*; Email: mohit.melwani.daswani@jpl.nasa.gov

Authors

Bing Hong Chua − *Jet Propulsion Laboratory, California Institute of Technology, Pasadena, California 91109, United States; Asian School of the Environment, Nanyang Technological University, Singapore 639798, Singapore;* orcid.org/0009-0002-1144-2368

Elodie Gloesener − *Jet Propulsion Laboratory, California Institute of Technology, Pasadena, California 91109, United States;* orcid.org/0009-0001-8340-3192

Mathieu Choukroun − *Jet Propulsion Laboratory, California Institute of Technology, Pasadena, California 91109, United States;* orcid.org/0000-0001-7447-9139

Tuan H. Vu − *Jet Propulsion Laboratory, California Institute of Technology, Pasadena, California 91109, United States;* orcid.org/0000-0001-6839-9765

Baptiste Journaux − *Department of Earth and Space Sciences, University of Washington, Seattle, Washington 98195, United States*

Marshall J. Styczinski − *Jet Propulsion Laboratory, California Institute of Technology, Pasadena, California 91109, United States*

Steven D. Vance − *Jet Propulsion Laboratory, California Institute of Technology, Pasadena, California 91109, United States*

Complete contact information is available at: https://pubs.acs.org/10.1021/acsearthspacechem.3c00091

Notes

The authors declare no competing financial interest.

■ ACKNOWLEDGMENTS

Part of this work has been conducted at the Jet Propulsion Laboratory, California Institute of Technology, under contract with the National Aeronautics and Space Administration (80NM0018D0004). Part of this work was supported by a NASA Planetary Science Early Career Award (NNH19ZDA001N-ECA) to M. Melwani Daswani. Support from the JPL Visiting Student Research Program is gratefully acknowledged. Government sponsorship is acknowledged. Reference herein to any specific commercial product, process, or service by trade name, trademark, manufacturer, or otherwise does not constitute or imply its endorsement by the United States Government or the Jet Propulsion Laboratory, California Institute of Technology. Copyright 2023 The Authors.

■ REFERENCES

(1) Tillner-Roth, R.; Friend, D. G. A Helmholtz Free Energy Formulation of the Thermodynamic Properties of the Mixture {Water + Ammonia}. *J. Phys. Chem. Ref. Data* **1998**, *27*, 63−96.

(2) Mousis, O. An Evolutionary Turbulent Model of Saturn's Subnebula: Implications for the Origin of the Atmosphere of Titan. *Icarus* **2002**, *156*, 162−175.

(3) Dodson-Robinson, S. E.; Willacy, K.; Bodenheimer, P.; Turner, N. J.; Beichman, C. A. Ice lines, planetesimal composition and solid surface density in the solar nebula. *Icarus* **2009**, *200*, 672−693.

(4) Hammond, N. P.; Parmenteir, E. M.; Barr, A. C. Compaction and Melt Transport in Ammonia-Rich Ice Shells: Implications for the Evolution of Triton. *J. Geophys. Res.: Planets* **2018**, *123*, 3105−3118.

(5) Shock, E. L.; McKinnon, W. B. Hydrothermal Processing of Cometary Volatiles−Applications to Triton. *Icarus* **1993**, *106*, 464−477.

(6) Castillo-Rogez, J. C.; Daswani, M. M.; Glein, C. R.; Vance, S. D.; Cochrane, C. J. Contribution of Non-Water Ices to Salinity and Electrical Conductivity in Ocean Worlds. *Geophys. Res. Lett.* **2022**, *49*, No. e2021GL097256.

(7) Miller, K. E.; Glein, C. R.; Waite, J. H. Contributions from Accreted Organics to Titan's Atmosphere: New Insights from Cometary and Chondritic Data. *Astrophys. J.* **2019**, *871*, No. 59.

(8) Singh, S. K.; Bergantini, A.; Zhu, C.; Ferrari, M.; Sanctis, M. C. D.; De Angelis, S.; Kaiser, R. I. Origin of ammoniated phyllosilicates on dwarf planet Ceres and asteroids. *Nat. Commun.* **2021**, *12*, No. 2690, DOI: 10.1038/s41467-021-23011-4.

(9) Cartwright, R. J.; Beddingfield, C. B.; Nordheim, T. A.; Roser, J.; Grundy, W. M.; Hand, K. P.; Emery, J. P.; Cruikshank, D. P.; Scipioni, F. Evidence for Ammonia-bearing Species on the Uranian Satellite Ariel Supports Recent Geologic Activity. *Astrophys. J.* **2020**, *898*, No. L22.

(10) Cook, J. C.; Ore, C. M. D.; Protopapa, S.; Binzel, R. P.; et al. Composition of Pluto's small satellites: Analysis of New Horizons spectral images. *Icarus* **2018**, *315*, 30−45.

(11) Desch, S. J.; Cook, J. C.; Doggett, T.; Porter, S. B. Thermal evolution of Kuiper belt objects, with implications for cryovolcanism. *Icarus* **2009**, *202*, 694−714.

(12) Waite, J. H.; Glein, C. R.; Perryman, R. S.; Teolis, B. D.; Magee, B. A.; Miller, G.; Grimes, J.; Perry, M. E.; Miller, K. E.; Bouquet, A.; et al. Cassini finds molecular hydrogen in the Enceladus plume: Evidence for hydrothermal processes. *Science* **2017**, *356*, 155−159.

(13) Pizzarello, S.; Williams, L. B.; Lehman, J.; Holland, G. P.; Yarger, J. L. Abundant ammonia in primitive asteroids and the case for a possible exobiology. *Proc. Natl. Acad. Sci. U.S.A.* **2011**, *108*, 4303−4306.

(14) Poch, O.; Istiqomah, I.; Quirico, E.; et al. Ammonium salts are a reservoir of nitrogen on a cometary nucleus and possibly on some asteroids. *Science* **2020**, *367*, No. 6483, DOI: 10.1126/science.aaw7462.

(15) Kargel, J. S. Ammonia-water volcanism on icy satellites: Phase relations at 1 atm. *Icarus* **1992**, *100*, 556−574.

(16) Fortes, A. D.; Choukroun, M. Phase Behaviour of Ices and Hydrates. *Space Sci. Rev.* **2010**, *153*, 185−218.

(17) Schoonen, M. A.; Xu, Y. Nitrogen Reduction Under Hydrothermal Vent Conditions: Implications for the Prebiotic Synthesis of C-H-O-N Compounds. *Astrobiology* **2001**, *1*, 133−142.

(18) Cockell, C. S.; Bush, T.; Bryce, C.; et al. Habitability: A Review. *Astrobiology* **2016**, *16*, 89−117.
(19) Chan, J. P.; Giauque, W. F. The Entropy of NH3·2H2O. Heat Capacity from 15 to 300 K.1. *J. Phys. Chem. A* **1964**, *68*, 3053−3057.
(20) Hildenbrand, D. L.; Giauque, W. F. Ammonium Oxide and Ammonium Hydroxide. Heat Capacities and Thermodynamic Properties from 15 to 300 K.1. *J. Am. Chem. Soc.* **1953**, *75*, 2811−2818.
(21) Zinner, K. The Heat Content of Mixtures of Ammonia and Water Dependent on the Composition and Temperature. *Z. Gesamt. Kalte-Ind.* **1934**, *41*, 21−29.
(22) Wrewsky, M.; Kaigorodoff, A. I. Wärmekapazität wässeriger Lösungen von Chlorwasserstoff und Ammoniak bei verschiedenen Temperaturen. *Z. Phys. Chem.* **1924**, *112U*, 83−89.
(23) Chernen'kaya, E. Heat capacity of solutions of electrolytes and their mixtures. I. Experimental determination of the heat capacity of aqueous solutions of ammonium bicarbonate, sodium bicarbonate, sodium carbonate, ammonia, and liquids for the soda production at 25 C. *Zh. Prikl. Khim.* **1971**, *44*, 1543−1549.
(24) Allred, G. C.; Woolley, E. M. Heat capacities of aqueous acetic acid, sodium acetate, ammonia, and ammonium chloride at 283.15, 298.15, and 313.15 K: ΔC°p for ionization of acetic acid and for dissociation of ammonium ion. *J. Chem. Thermodyn.* **1981**, *13*, 155−164.
(25) Fujita, I.; Suzuki, T.; Uematsu, M. Isobaric specific heat capacity of {xH2O+(1- x) NH3} with x = (0.0000, 0.1566, 0.1597, 0.3030, 0.3048, 0.4956, 0.7061, and 0.8489) at T = (280, 300, 320, and 360) K over the pressure range from (0.1 to 15) MPa. *J. Chem. Thermodyn.* **2008**, *40*, 260−264.
(26) Prieto-Ballesteros, O.; Muñoz-Iglesias, V.; Bonales, L. J. Heat storage in ocean worlds: The role of slurries. *Mon. Not. R. Astron. Soc.* **2022**, *515*, 3512−3523.
(27) Osborne, N. S.; van Dusen, M. S. Specific Heat of Liquid Ammonia. *J. Am. Chem. Soc.* **1918**, *40*, 1−13.
(28) Tillner-Roth, R.; Friend, D. G. Survey and Assessment of Available Measurements on Thermodynamic Properties of the Mixture {Water + Ammonia}. *J. Phys. Chem. Ref. Data* **1998**, *27*, 45−61.
(29) Committee on the Planetary Science and Astrobiology Decadal Survey; Space Studies Board; Division on Engineering and Physical Sciences; National Academies of Sciences, Engineering, and Medicine. *Origins, Worlds, and Life: A Decadal Strategy for Planetary Science and Astrobiology 2023−2032*, National Academy of Sciences202226522.
(30) Croft, S. K.; Lunine, J. I.; Kargel, J. Equation of state of ammonia-water liquid: Derivation and planetological applications. *Icarus* **1988**, *73*, 279−293.
(31) Vu, T. H.; Piqueux, S.; Choukroun, M.; Edwards, C. S.; Christensen, P. R.; Glotch, T. D. Low-temperature specific heat capacity measurements and application to Mars thermal modeling. *Icarus* **2019**, *321*, 824−840.
(32) Kousksou, T.; Jamil, A.; Zeraouli, Y. Enthalpy and apparent specific heat capacity of the binary solution during the melting process: DSC modeling. *Thermochim. Acta* **2012**, *541*, 31−41.
(33) Muñoz-Iglesias, V.; Choukroun, M.; Vu, T. H.; Hodyss, R.; Mahjoub, A.; Smythe, W. D.; Sotin, C. Phase Diagram of the Ternary Water−Tetrahydrofuran−Ammonia System at Low Temperatures. Implications for Clathrate Hydrates and Outgassing on Titan. *ACS Earth Space Chem.* **2018**, *2*, 135−146.
(34) Feistel, R.; Wagner, W. A New Equation of State for H2O Ice Ih. *J. Phys. Chem. Ref. Data* **2006**, *35*, 1021−1047.
(35) Journaux, B.; Brown, J. M.; Pakhomova, A.; Collings, I. E.; Petitgirard, S.; Espinoza, P.; Ballaran, T. B.; Vance, S. D.; Ott, J.; Cova, F.; Garbarino, G.; Hanfland, M. Holistic Approach for Studying Planetary Hydrospheres: Gibbs Representation of Ices Thermodynamics, Elasticity, and the Water Phase Diagram to 2, 300 MPa. *J. Geophys. Res.: Planets* **2020**, *125*, No. e2019JE006176, DOI: 10.1029/2019JE006176.
(36) Bollengier, O.; Brown, J. M.; Shaw, G. H. Thermodynamics of pure liquid water: Sound speed measurements to 700 MPa down to the freezing point, and an equation of state to 2300 MPa from 240 to 500 K. *J. Chem. Phys.* **2019**, *151*, No. 054501.
(37) Staudt, H. J. Dissertation, Universität Kaiserslautern, 1984.
(38) Shomate, C. H. A method for evaluating and correlating thermodynamic da ta. *J. Phys. Chem. A* **1954**, *58*, 368−372.
(39) Wagner, W.; Pruß, A. The IAPWS formulation 1995 for the thermodynamic properties of ordinary water substance for general and scientific use. *J. Phys. Chem. Ref. Data* **2002**, *31*, 387−535.
(40) Gallo, P.; Amann-Winkel, K.; Angell, C. A.; et al. Water: A Tale of Two Liquids. *Chem. Rev.* **2016**, *116*, 7463−7500.
(41) Journaux, B.; Brown, J. M.; Abramson, E.; Vance, S.*The Thermodynamics of Ammonia Rich Planetary Oceans: Equation of State for Water-Ammonia and Water-Ammonia-Salt Solutions from Surface to Abyssal Conditions*, AGU Fall Meeting Abstracts, 2021P44A-08.
(42) Brown, J. M. Local basis function representations of thermodynamic surfaces: Water at high pressure and temperature as an example. *Fluid Phase Equilib.* **2018**, *463*, 18−31.
(43) Archer, D. G. Thermodynamic Properties of the NaCl+H2O System. II. Thermodynamic Properties of NaCl(aq), NaCl·2H2(cr), and Phase Equilibria. *J. Phys. Chem. Ref. Data* **1992**, *21*, 793−829.
(44) Driesner, T. The system H2O-NaCl. Part II: Correlations for molar volume, enthalpy, and isobaric heat capacity from 0 to 1000 °C, 1 to 5000 bar, and 0 to 1 XNaCl. *Geochim. Cosmochim. Acta* **2007**, *71*, 4902−4919.
(45) Vance, S. D.; Panning, M. P.; Stähler, S.; Cammarano, F.; Bills, B. G.; Tobie, G.; Kamata, S.; Kedar, S.; Sotin, C.; Pike, W. T.; Lorenz, R.; Huang, H.-H.; Jackson, J. M.; Banerdt, B. Geophysical Investigations of Habitability in Ice-Covered Ocean Worlds. *J. Geophys. Res.: Planets* **2018**, *123*, 180−205.
(46) Styczinski, M. J.; Vance, S. D.; Daswani, M. M. PlanetProfile: Self-consistent interior structure modeling for terrestrial bodies in Python, 2022.
(47) Lemmon, E. W.; Bell, I. H.; Huber, M. L.; McLinden, M. O.; National Institute of Standards and Technology. NIST Standard Reference Database 23: Reference Fluid Thermodynamic and Transport Properties-REFPROP, Version 10.0, 2018 https://www.NIST.gov/srd/refprop.
(48) Buffo, J. J.; Meyer, C. R.; Parkinson, J. R. G. Dynamics of a Solidifying Icy Satellite Shell. *J. Geophys. Res.: Planets* **2021**, *126*, No. e2020JE006741, DOI: 10.1029/2020JE006741.
(49) Vance, S. D.; Journaux, B.; Hesse, M.; Steinbrügge, G. The Salty Secrets of Icy Ocean Worlds. *J. Geophys. Res.: Planets* **2021**, *126*, No. e2020JE006736, DOI: 10.1029/2020JE006736.

https://doi.org/10.1021/acsearthspacechem.3c00091
ACS Earth Space Chem. 2023, 7, 1971−1979